REPORT DOCUMENTATION PAGE

Form Approved
OMB No. 0704-0188

1. REPORT DATE *(DD-MM-YYYY)*	**2. REPORT TYPE**	**3. DATES COVERED** *(From - To)*
27 July 2016	Conference Paper	30 June 2016 - 27 July 2016

4. TITLE AND SUBTITLE
Supercritical Mixing in a Shear Coaxial Injector

5a. CONTRACT NUMBER

5b. GRANT NUMBER

5c. PROGRAM ELEMENT NUMBER

6. AUTHOR(S)
Sardeshmukh, S., Anderson, W., Harvazinski, M. and Sankaran, V.

5d. PROJECT NUMBER

5e. TASK NUMBER

5f. WORK UNIT NUMBER
Q12J

7. PERFORMING ORGANIZATION NAME(S) AND ADDRESS(ES) AND ADDRESS(ES)

Air Force Research Laboratory (AFMC)
AFRL/RQR
5 Pollux Drive
Edwards AFB, CA 93524-7048

8. PERFORMING ORGANIZATION REPORT NO.

9. SPONSORING / MONITORING AGENCY NAME(S) AND ADDRESS(ES)

Air Force Research Laboratory (AFMC)
AFRL/RQR
5 Pollux Drive
Edwards AFB, CA 93524-7048

10. SPONSOR/MONITOR'S ACRONYM(S)

11. SPONSOR/MONITOR'S REPORT NUMBER(S)
AFRL-RQ-ED-TP-2016-199

12. DISTRIBUTION / AVAILABILITY STATEMENT
Approved for Public Release; Distribution Unlimited. PA Clearance Number: 16328 Clearance Date: 7/12/2016

13. SUPPLEMENTARY NOTES
For presentation at AIAA Propulsion and Energy Conference 2016; Salt Lake City, UT July 25-27, 2016

14. ABSTRACT

Supercritical mixing of nitrogen is explored in a shear coaxial injector using detached eddy simulations with the Peng-Robinson equation of state. Computational results are processed and compared against experimental data. Time averaged results are shown to agree well with the experimental temperature profile near the tip of the injector. The transient flowfield is captured with shadowgraph images generated from the simulation and compared with the experimental images. Distinctive features of the shear coaxial flow are identified including high density inner core, the outer jet flow and shear layer between the outer injector fluid and the co-flow. These features are reasonably duplicated in the computational shadowgraph images. Shadowgraph images are found to depend on the distance of the screen from the fluid domain and therefore inferences drawn from such images are associated with this distance. Further, comparison of the shadowgraph images with a slice of the flowfield may not compare the same features and are found to be of limited use for the purpose of validation. Mixing length of the dense flow in the core of the injected fluid emphasizes this observation. Two acoustically excited cases: pressure node and pressure anti-node at the center plane of the jet are also studied in the same manner. The pressure anti-node case shows puffing behavior that does not significantly disrupt the inner core, while the pressure node case generates flapping motion which perceptibly shortens the core flow of the injected jet.

15. SUBJECT TERMS
N/A

16. SECURITY CLASSIFICATION OF:			**17. LIMITATION OF ABSTRACT**	**18. NUMBER OF PAGES**	**19a. NAME OF RESPONSIBLE PERSON**
					V. Sankaran
a. REPORT	**b. ABSTRACT**	**c. THIS PAGE**	SAR	16	**19b. TELEPHONE NO** *(include area code)*
Unclassified	**Unclassified**	**Unclassified**			N/A

Standard Form 298 (Rev. 8-98)
Prescribed by ANSI Std. 239.18

Supercritical Mixing in a Shear Coaxial Injector

S. V. Sardeshmukh[1], W. E. Anderson[2]
Purdue University, W. Lafayette, IN 47906

M. E. Harvazinski[3], V. Sankaran[4]
AFRL, Edwards AFB, CA 93524

Supercritical mixing of nitrogen is explored in a shear coaxial injector using detached eddy simulations with the Peng-Robinson equation of state. Computational results are processed and compared against experimental data. Time averaged results are shown to agree well with the experimental temperature profile near the tip of the injector. The transient flowfield is captured with shadowgraph images generated from the simulation and compared with the experimental images. Distinctive features of the shear coaxial flow are identified including high density inner core, the outer jet flow and shear layer between the outer injector fluid and the co-flow. These features are reasonably duplicated in the computational shadowgraph images. Shadowgraph images are found to depend on the distance of the screen from the fluid domain and therefore inferences drawn from such images are associated with this distance. Further, comparison of the shadowgraph images with a slice of the flowfield may not compare the same features and are found to be of limited use for the purpose of validation. Mixing length of the dense flow in the core of the injected fluid emphasizes this observation. Two acoustically excited cases: pressure node and pressure anti-node at the center plane of the jet are also studied in the same manner. The pressure anti-node case shows puffing behavior that does not significantly disrupt the inner core, while the pressure node case generates flapping motion which perceptibly shortens the core flow of the injected jet.

I. Introduction

ROCKET engines present a unique environment for injection of the propellants due to their extreme pressure and temperature conditions, especially for cryogenic propellants. The high pressure and low temperature conditions of these propellants can span the sub-, trans- and super-critical regimes of the fluids, requiring the use of real gas equations of state. Additionally, the high volumetric rates of energy release make these engines susceptible to acoustic excitation. The acoustics can couple with the fluid dynamics of the injection leading to mixture perturbations, which can result in combustion instabilities. Such issues typically appear at a later stage in the design process and can severely affect the overall timeline and expenditure of rocket engine development programs. The unsteady mixing process under super-critical pressures is therefore of key importance to the the design of rocket injectors.

Recent advances in various fields have made it a necessity to re-examine the process of developing rocket engines. Of particular note are the material science and manufacturing techniques that now allow fabrication of unique injector shapes that are otherwise not feasible. This is also spurred on by involvement of private corporations in the area of space propulsion. However, these factors have yielded limited overall progress because the existing design practices - based mainly on the experiments are limited in the understanding of the fluid dynamics and combustion. It is therefore important to improve the understanding of rocket injectors with well validated high fidelity computations to understand the physics.

---

[1] Post-doctoral Research Assoc., Aeronautics & Astronautics, 124 Chaffee Hall, 500 Allisson Road, AIAA Member.
[2] Professor, Aeronautics and Astronautics, 701 W. Stadium Ave., Associate Fellow, AIAA.
[3] Scientist, Rocket Propulsion Division, Air Force Research Laboratory (AFRL), Member, AIAA.
[4] Senior Scientist, Rocket Propulsion Division, Air Force Research Laboratory (AFRL), Member, AIAA.

The injection of cryogenic propellants is common to various liquid rocket engines such as SSME, Vulcain and others [1]. At these conditions for the oxygen/hydrogen propellant combination with shear co-axial injection, the inner jet is typically oxygen at a sub-critical temperature and supercritical pressure while the outer jet of hydrogen is injected at supercritical pressure and temperature owing to its low critical temperature as well as its use for regenerative cooling purposes. Experimental studies of similar injectors with variations in the injector geometry and operating conditions have been conducted by several researchers [1-6]. Some of these studies were focused on non-reactive flows [7] in order to eliminate the complexities introduced due to multi-component reactive mixtures. The studies by Leyva et al., and Rodriguez et al. also considered the impact of acoustic excitation on the length of the high density region, which is an important characteristic along with the spreading angle of the jet [8]. The experimental techniques used for these studies include back-lit or shadowgraph images, Raman measurements, and ultraviolet emission band measurements in the case of reacting flows. Out of these measurement techniques, the Raman measurements can provide density measurements in a cross section but the other measurement techniques provide mostly qualitative data. The objective of the present paper is perform detailed simulations of both unforced and acoustically forced shear-coaxial injector flowfields and to make careful assessments of the method of comparing the predicted data with the available experimental measurements.

Some of the experiments have been previously numerically investigated to understand the shear layer dynamics in supercritical injection at rocket engine conditions [2, 9, 10]. The presence of recirculation zones on the injector face has been noted as an important feature of the supercritical co-axial injection. Spectral content has also been investigated for the experiments and simulations, quantifying the interaction of the flow and the imposed acoustic field [8, 10]. The energetic structures believed to be responsible for the observations and thus hypothesized mixing trends in the experiments have been investigated by Teshome et al. [3] and the dynamic response of these structures from experimental images of similar cases is examined by Hua et al. [11]; but corresponding computational simulations have not yet been performed.

The remainder of the paper is organized as follows. We begin by describing the computational solver including the treatment of the real fluid and the details of the experiment that is being analyzed. The post-processing method for generating computational shadowgraph images for comparison with the experimental shadowgraphs is also discussed. We then present the results and validation for three cases: a baseline case and two acoustically excited cases are shown. Lastly, conclusions and directions for future efforts are given.

II. Modeling Details

A. Computational Solver and Equation of State

An in-house Navier-Stokes solver – General Equation and Mesh Solver (GEMS) is used. It is an implicit dual time-stepping fully-coupled solver with low Mach number preconditioning that uses a detached eddy simulations (DES) for turbulence modeling [12-14]. The GEMS framework is developed for arbitrary equations of state and caloric relations, which makes it a suitable platform for implementing the real gas equations necessary in the present study. The solver is also capable of handling the multi-step detailed chemical kinetics along with correction terms for high-pressures. For these studies, a single-fluid model is used to describe the fluid properties using the Peng-Robinson equation of state (PR-EOS). The PR-EOS is chosen for its relatively simple implementation and better accuracy than the Redlich-Kwong equations of state [15]. The Redlich-Kwong EOS is known to underpredict the density in the sub-critical regions due to overprediction of the critical compressibility factor [16]. It is known that in spite of better accuracy, the critical compressibility prediction with PR-EOS remains higher than the experimental values, which affects the sub-critical and near-critical regions. In the present study, these regions are not encountered.

The real gas effects are included in this model using the compressibility factor Z. The compressibility is computed as a cubic root of the equation

$$Z^3 - a_2 Z^2 + a_1 Z + a_0 = 0, \tag{0.1}$$

here the coefficients a_0, a_1 and a_2 are given as

$$\begin{aligned} a_2 &= -(1-B) \\ a_1 &= A - 3B^2 - 2B \\ a_0 &= -AB + B^2 + B^3, \end{aligned} \tag{0.2}$$

where A and B are the cubic parameters dependent on the species properties and critical pressure and temperature, defined as,

$$A = a_m \frac{P}{\left(RT\right)^2} \qquad B = b_m \frac{P}{RT} \tag{0.3}$$

Here, P and T are pressure and temperature respectively, R is the universal gas constant and a_m and b_m are the mixture properties calculated using the mixing laws,

$$a_m = \sum_{i=1}^{NS}\sum_{j=1}^{NS} X_i X_j a_{i,j} k_{i,j} \qquad b_m = \sum_{i=1}^{NS} X_i b_i \tag{0.4}$$

In this expression, X_i are the mole fractions of species *i*, $k_{i,j}$ are the binary interaction parameters for the species *i* and *j*, b_i is a critical property dependent constant; and $a_{i,j}$ is calculated using the mixing rule,

$$a_{i,j} = \sqrt{a_i a_j} \tag{0.5}$$

where again the constants a_i are dependent on critical properties. These mixing rules are used by Soave [17] for the Redlich-Kwong equation of state and are adequate for the Peng-Robinson equation of state [16]. The terms a_i and b_i are given as,

$$a_i = a_c \left(RT_{c,i}\right)\left(1+\kappa_i\left(1-T_{r,i}\right)\right)^2 \qquad b_i = b_c \frac{RT_{c,i}}{P_{c,i}} \tag{0.6}$$

where P_c and T_c are the critical pressure and temperature of the fluid. The constants in this equation are:

$$\begin{aligned} &a_c = 0.45724, \quad b_c = 0.0778; \\ &\kappa = k_0 + k_1\omega_i + k_2\omega_i^2; \\ &k_0 = 0.37464; \quad k_1 = 1.54226; \quad k_2 = -0.2699 \end{aligned} \tag{0.7}$$

with ω as the acentricity factor and the reduced temperature T_r is obtained via,

$$T_r = \sqrt{\frac{T}{T_c}} \tag{0.8}$$

The remaining terms such as enthalpy, entropy and respective derivatives are computed as departure functions from the ideal gas law.

A plot of density computed with the Peng-Robinson equation of state (EOS) is shown in **Figure 1**. The computed density is compared against the values obtained from NIST REFPROP program and found to be in reasonable agreement for the temperature range of interest [18].

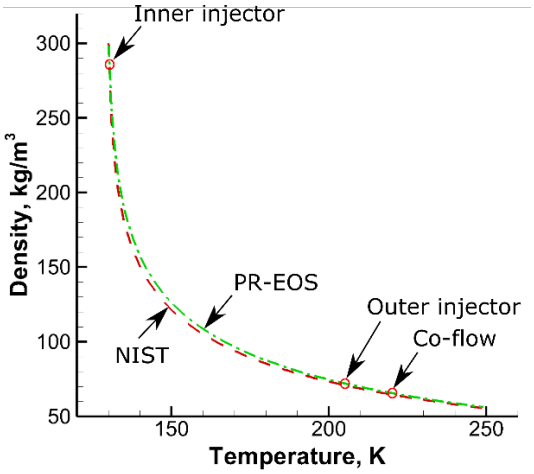

Figure 1. Comparison of density computed with PR-EOS and obtained from NIST database[18].

B. Computational Shadowgraph

Computations can provide a significant advantage for understanding the underlying flow physics, but they require a careful assessment of the validity of the results. Although many quantities are available through computations to compare against the measurements, a direct comparison often benefits the validity assessment. The experiments that are referenced in the present study have recorded back-lit or shadowgraph images. It is therefore important to follow the same process and obtain the shadowgraph images from computed density field. The computational procedure that is used here is described by Yates in the literature [19]. This method is implemented by Saunders and Kennelly and is available as an open source utility [20].

The details of the method are included here for reference. The method assumes a discretized, perfectly collimated source of light with unit intensity. Given the density field and gradients from the computational solution, the refractive index of a gas is given by,

$$n = 1 + \kappa\rho \ , \tag{0.9}$$

where n is the refractive index, ρ is the density and κ is the Gladstone-Dale constant ($2.25\times10^{-4}\,\mathrm{m}^3/\mathrm{kg}$ for air). The angular deflections of light rays in a plane of the image are given by,

$$\begin{aligned} \delta\varepsilon_x &= \frac{1}{n}\frac{\partial n}{\partial x} \\ \delta\varepsilon_y &= \frac{1}{n}\frac{\partial n}{\partial y} \end{aligned} \tag{0.10}$$

where $\delta\varepsilon_x$ and δ_y are the deflections. Line integral of the deflections then gives the total deflection of a ray in a cell as,

$$\delta_{i,j} = \int_{Z_k}^{Z_{k+1}} f\left[n(x,y,\zeta)\right] d\zeta \tag{0.11}$$

where the function f is dependent on the type of image desired. A shadowgraph requires the magnitude of the deflections given in equation (1.10). Summation of these line integrated deflections through the path of a ray gives the total deflection across the fluid domain. However, it was noted by Yates that a spline integration within a cell is computationally expensive and yields insignificant benefit in comparison to the straight line assumption. The procedure by Saunders and Kennelly thus assumes that, inside a computational cell, the ray traverses a straight path. After exiting the computational domain, the deflected rays are projected onto a screen as shown in **Figure 2**.

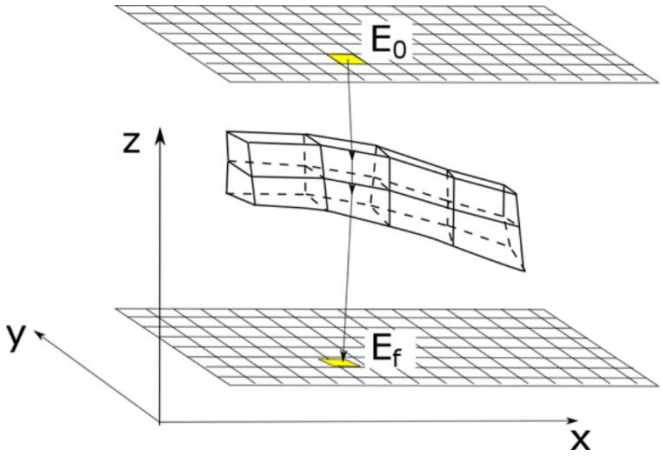

Figure 2. Schematic of the computational shadowgraph technique. Original intensity given by E_0 and the deflection of the projected rays on the screen gives overlap with cells, which is used for computing the change in intensity $\Delta E_{i,j}$ at the cell (i, j) of the image.

The original light source is assumed to be collection of discrete elements of light and the corners of each light element are assumed to be perfectly collimated rays of light. These rays pass through the flowfield and are distorted due to the changes in refractive index. After exiting the flowfield, assuming no further deflections, the rays bounding each light element are projected on the shadowgraph screen, producing a distorted image of the original element of light. The superposition of such distorted projections on the screen gives the intensity at a given cell or "pixel" on the screen. The change in intensity due to such projections is computed as,

$$\Delta E_{i,j} = E_0 \left(\frac{A_f \cap A_{i,j}}{A_0} \right) \tag{0.12}$$

where E_0 is the original intensity, A_0 is the original area of the light element, $A_{i,j}$ is the area of the screen cell and A_f is the area of the distorted light element. The sum total of these small changes gives the intensity at a given point on the shadowgraph screen.

$$E_{i,j} = \sum_{n=1}^{N} \Delta E_{i,j} \quad . \tag{0.13}$$

C. Computational Setup

The configuration chosen for the present study is described by Schmitt et al. and shown in **Figure 3**. It consists of a shear co-axial injector mounted in a perforated plate at the top of a chamber of rectangular cross section. The entire chamber is installed in a secondary pressurized container to maintain the elevated pressure condition. At the bottom, a circular hole acts as an outlet to the injected fluid, discharging into the outer chamber. The shear co-axial injector consists of inner injector of $d_i = 0.51$ mm diameter, which is recessed by $1/2\, d_i$ within the outer injector of diameter $d_o = 2.42$ mm. The injector assembly is offset from the mounting plate by 5 mm. Remaining features of the arrangement are as shown in the Figure 3.

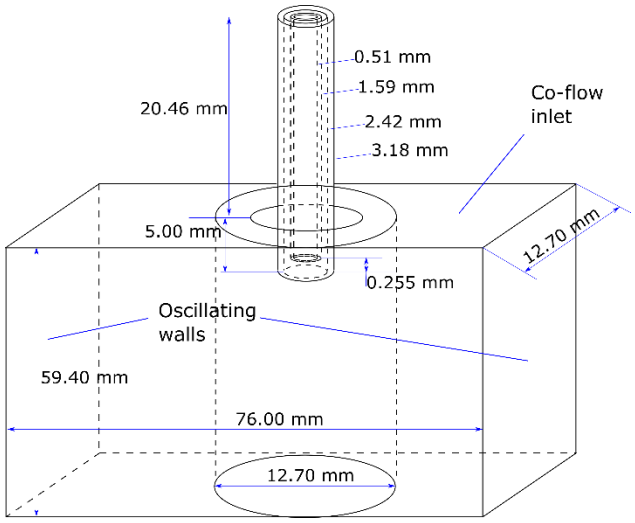

Figure 3. Experimental setup of the AFRL mixing study described by Schmitt et al. [2].

The grid is set up to have good spatial resolution near the injector tip and within the shear layers. The cell size in this region of interest is close to 10 μm with aspect ratios nearly unity. Downstream of the injector, near the outlet boundary, it is limited to 50 μm in cross section and 80 μm in axial direction. The total number of cells is 3.3 million and the mesh is divided into 480 partitions for solution. The blocking strategy and several cross sections of the mesh are shown in **Figure 4**.

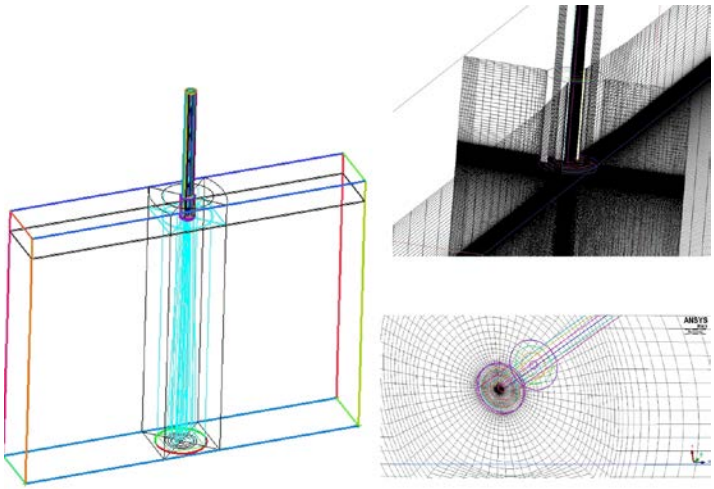

Figure 4. Blocking strategy and grid cross sections.

D. Boundary Conditions and Parameters

The time step is chosen as 1 μs so as to achieve more than an order of magnitude convergence within the sub-iterations. At the upstream boundary, the mass flow rate of nitrogen is specified as 8 mg/s for the outer injector and 0.8 mg/s for the inner injector. The main difference between the two boundary conditions is the temperature of the fluid, which is 137 K for the inner injector and 206 K for the outer injector. A reservoir-type condition is specified at the mounting plate to simulate the perforations in the experimental arrangement. The pressure at this boundary is specified to be 0.1% higher than the mean value and the co-flow velocity in the simulations is ascertained to be less than 1% of the jet velocity. At the downstream boundary, back-pressure is specified to be the same as the chamber condition. This condition is selected for its relatively smaller flow-through time so as to reduce the transient simulation time necessary. In addition to the baseline case, two acoustic excitation cases that employ oscillating side walls ae also studied. This approach is the same as that used in some of the previous work as well as related transverse instability studies [2, 21]. The experimental measurements of these cases showed pressure fluctuations

with amplitudes below 2% of the mean condition for the pressure antinode case and below 1% for the pressure node case. The boundary conditions for all three cases are summarized in **Table 1.**

Table 1. Boundary conditions specified for the three cases.

Boundary	P0	T0	mdot	K	w	Pback	Velocity	Frequency	Phase
Baseline – no acoustic excitation									
Inner injector	-	137	0.0008	0.54	3.15e5	-	-	-	-
Outer injector	-	206	0.008	2.47	9.69e6	-	-	-	-
Co-flow	5.0096	220	-	0.01	1.00e4	-	-	-	-
Outlet	-	-	-	-	-	4.96e6	-	-	-
Side wall	-	-	-	-	-	-	-	-	-
Acoustic excitation – pressure node									
Inner injector	-	137	0.0008	0.54	3.15e5	-	-		
Outer injector	-	206	0.008	2.47	9.69e6	-	-		
Co-flow	5.0096	220	-	0.01	1.00e4	-	-		
Outlet	-	-	-	-	-	4.96e6	-	-	-
Side wall	-	-	-	-	-	-	1.0	3000	0
Acoustic excitation – pressure antinode									
Inner injector	-	137	0.0008	0.54	3.15e5	-	-	-	-
Outer injector	-	206	0.008	2.47	9.69e6	-	-	-	-
Co-flow	5.0096	220	-	0.01	1.00e4	-	-	-	-
Outlet	-	-	-	-	-	4.96e6	-	-	-
Side wall	-	-	-	-	-	-	1.3	3000	180

III. Results and Discussion

The coaxial injectors flowing supercritical nitrogen have a temperature difference of 69 K. **Figure 5** shows the variation of the density of nitrogen as a function of pressure and temperature. Real gas effects become important in this regime as the temperature difference in this case leads to a density difference of 200 kg/m^3 or higher. The injector sets up two shear layers, the first one between the two injectors and the second between the small amount of co-flow and the outer injector. Mixing of the inner dense jet and the outer jet representative of the fuel is of primary interest and has been the focus of the experimental investigations. In addition to the images, the time-averaged temperature field near the tip of the injector was also probed in the experiments.

In the present work, we start with time-averaged results for the baseline case. The computed density field is then post-processed to generate shadowgraph images for comparison. Several features of interest including the two shear layers are observed from these comparisons, which are conducted for the three computational cases. The fluid dynamic features observed in shadowgraphs are then discussed.

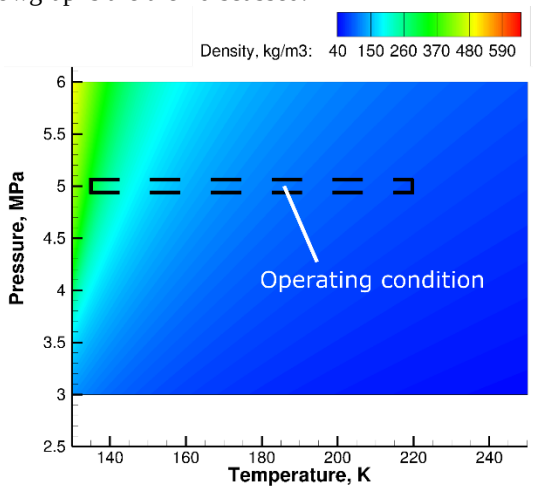

Figure 5. Dependence of nitrogen density on pressure and temperature.

A. Time-Averaged Flowfield

Time-averaging is started after two flow-through times and continued for four flow-through times, which gives statistically relevant information. The averaged temperature and density contours are shown in the **Figure 6**. The observed density contour is seen to favorably compare with the experimental average. It is seen from these plots that the inner jet core in a time averaged sense persists up to 5 diameters downstream of the injector. The temperature contour shows a slight difference from the density field. Recalling that the density variation shown in **Figure 1** indicated a rapid change in density up to a temperature of 150 K, this difference is expected. A slight contraction is seen close to the injector tip from the experimental image. This is a result of the co-flow entrainment in the outer shear layer, but the limited contrast at these density levels provides an insufficiently distinct outline in the experimental image. The computed temperature field shows this contraction. The outer shear layer length from this plot is seen to be slightly greater than 15 inner jet diameters.

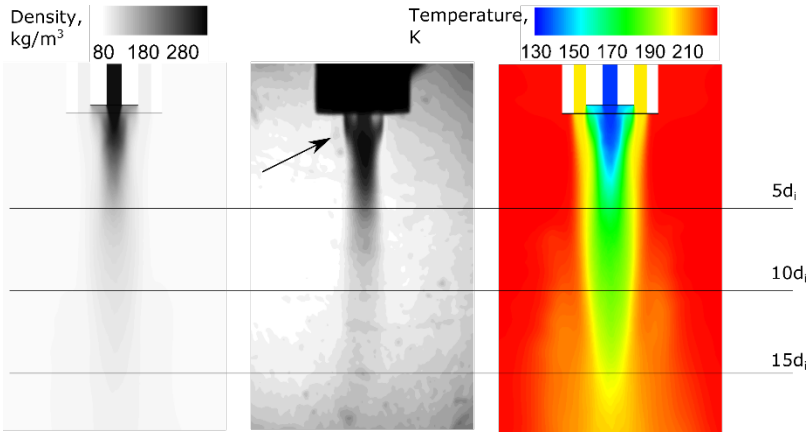

Figure 6. Time averaged temperature and density field at the center plane compared to the average experimental image (center).

In addition to the qualitative comparisons, time averaged temperature data is available from the experiments. This is compared against the simulation in **Figure 7**. For this comparison, it should be noted that the thermocouple tip was of 0.1 mm diameter, the readings are 0.1 to 0.05 mm apart and the measurements were at a distance less than one injector diameter (~ 0.3 mm) downstream of the inner injector[7]. This allows relatively few readings across the inner injector and the inner shear layer. The simulation data was mass averaged within a representative convex zone to mimic the measurements. The comparison shows that there is reasonable agreement with the measurements. Some difference is observed, especially in the region of sharp temperature gradients. However, given the dimension of the inner injector and the probe, such difference may be a result of uncertainties in the position of the probe in either the experiment or computations.

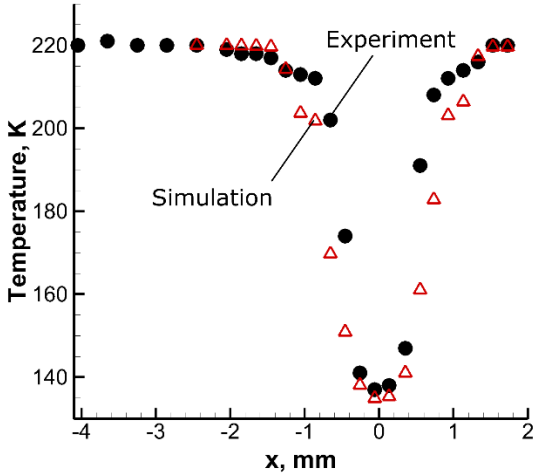

Figure 7. Time averaged temperature comparison with data at one inner jet diameter downstream of the injector.

B. Transient Flowfield

The transient phenomena dominating the flowfield are captured in series of images from the experiment. As described in section IIB, the computational density field is processed to obtain a shadowgraph image. This image contains many light and dark spots that are formed due to the overlapping of the distorted projections of light elements onto the screen. In the experimental image, the innermost dark region is expected to represent the high density core jet. Additionally, upon closer examination, the outer injector flow and the shear layer between the outer flow and co-flow can also be observed. **Figure 8** shows the comparison between experimental and computational shadowgraph images for a given instance of time. The number of dark and light spots as well as their shape is slightly dependent on the number of light elements employed. The computational images are generated with 7680x12480 or approximately 95 million light sources. This level of resolution gives sharp contrast but is computationally expensive, requiring 2 hours of computing time per image. For the remainder of the paper, the number of light sources is reduced to 1920x3120 to facilitate rendering within a reasonable period of time.

The three regions: the dark core, outer injector flow and outer shear layer are marked on the experimental image by the dashed, closely dotted and sparsely dotted lines. These same outlines are superimposed on the computational shadowgraph to establish the correspondence between these two images. The comparison suggests that the structures formed in the computational shadowgraph closely resemble the experimental observations. Various nuances of the outer injector flow are also observed from the computational image. There is however, some difference in the light intensity, which makes the core appear significantly dark in the experiment in comparison to outlying regions. This discrepancy is related to the screen distance as discussed in the next section.

The transient flowfield is further assessed by comparing two subsequent time instances. These are shown in **Figure 9**. The marked regions from experimental images show a close resemblance to the structures observed in the computational shadowgraphs. This signifies the temporal similarity between the computations and experiments.

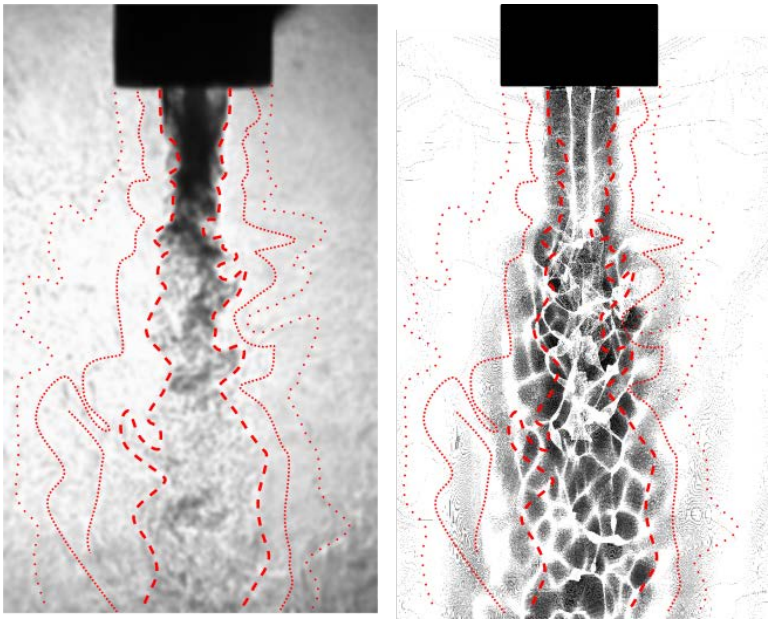

Figure 8. Transient flowfield captured by experimental and computational shadograph image. Outlines of inner dark region(--), outer injector flow(…) and shear layer between co-flow and outer injector (. . .) are identified for the experiment and then superimposed on the computational image.

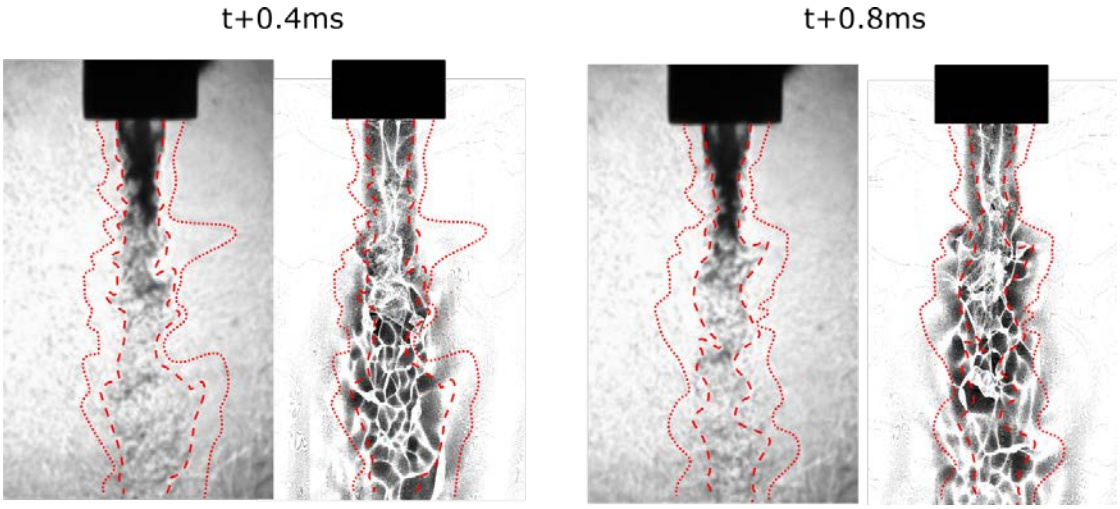

Figure 9. Experimental and computational shadograph images of two subsequent time instances. Outlines of inner dark region(--), outer injector flow(…) are marked on the experimental image and then superimposed on the computational image.

C. Impact of Screen Distance

Although qualitative similarity is apparent from the above images, differences in the light intensity are also evident. It is important to understand such differences in a direct comparison. In this case, an important parameter is the distance of the screen from the experimental arrangement. This distance is varied in the computational shadowgraph and the resulting differences are shown in **Figure 10**. At the shortest distance of 1 cm, many of the prominent features of the downstream flow cannot be identified. The upstream features of the flow, on the other hand, are clearly seen and the two shear layers can be observed. At a distance of 10 cm, the outline of the dark inner region is apparent and the first few oscillations can similarly be seen. The clarity of the upstream flowfield starts to diminish at this distance and the outer injector flow appears darker. This trend is seen to continue at 25 cm, which corresponds to the experimental distance. Recall that the computational shadowgraph procedure projects deflected light on the screen and the intensity at a given location on the screen is dependent on the superposition of all deflected light elements reaching that position. This explains how the bright spot in the image formed at a distance of 10 cm transforms to darker region at 25 cm. Finally at the extreme screen distance of 100 cm, a large portion of the inner core as well as the shear layer appear very dark while some of the downstream structures appear bright.

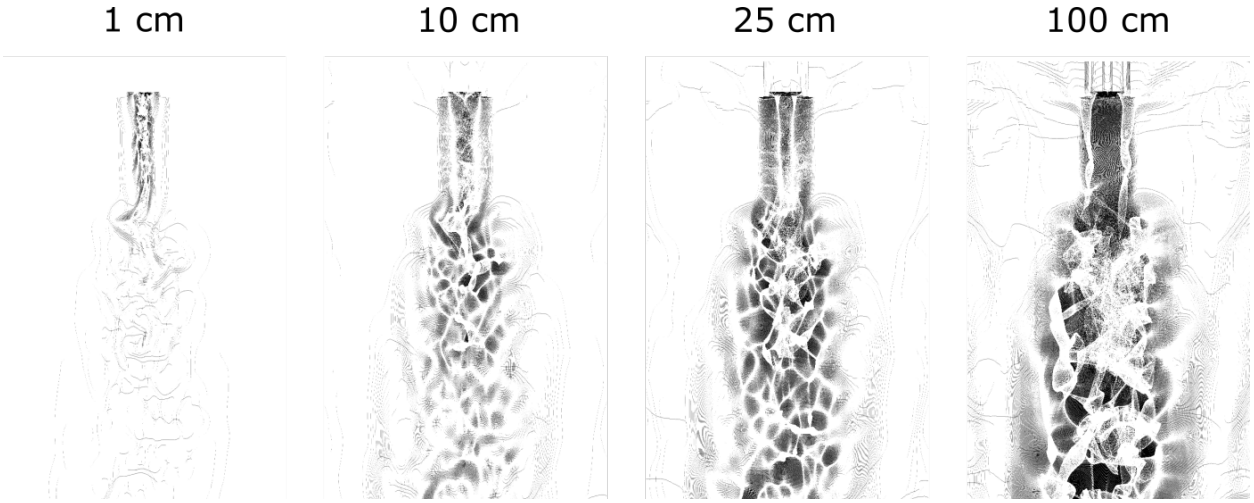

Figure 10. Computational shadograph images of the flowfield at varying distance of the screen from the fluid domain. The images are formed by computing deflections of discrete light elements through the flowfield and the intensity is obtained by superposition of projected light onto a screen.

As per our expectation, the best correspondence between the experiments and computations is obtained with the screen distance of 25 cm. An implication of this observation is that the dark core in the experimental image is related to the distance of the screen if the procedure is similar. To assess this statement, **Figure 11** compares details of computed flowfield with the experimental image.

The first comparison shown in **Figure 11** highlights the difference between a section of the flowfield and the line averaged image captured in the experiment. This establishes the need to achieve direct comparison between experiments and simulation for the purpose of validation of the latter. Second detail shown in **Figure 11**(c) shows the iso-surface of the density at three levels; the highest level (300 kg/m^3) shows the inner core flow. The core flow is thus seen to be heated up and partially mixed with the outer flow within a short distance, dropping the density to nearly two thrid or 180 kg/m^3. The last iso-surface at 90 kg/m3 shows the outer shear layer between the outer injector and the co-flow. Comparison with the experimental image shows that structures observed beyond the presence of the dark core can be in this case due to the complex fluid flow. Such flow structures can act to deflect the light in the same manner as some of the higher density gradients near the core flow. If such regions occur contiguously with the high density flow, the shadowgraph images may not be representative of the fluid flow.

The last plot, **Figure 11**(d) focuses on the mixing of the inner and outer jets. The fluids through the two injectors are tagged so as to enable such an investigation. A line contour of 80% inner fluid is shown in black, indicating the intact core flow. The drop in the inner fluid mass fraction to 50% is shown by the blue iso-surface while the brown line contour is that of 80% of the outer fluid. Comparing this with the dark region shown in the experimental image, 50% mixing is seen to occur at nearly twice the length of the dark core.

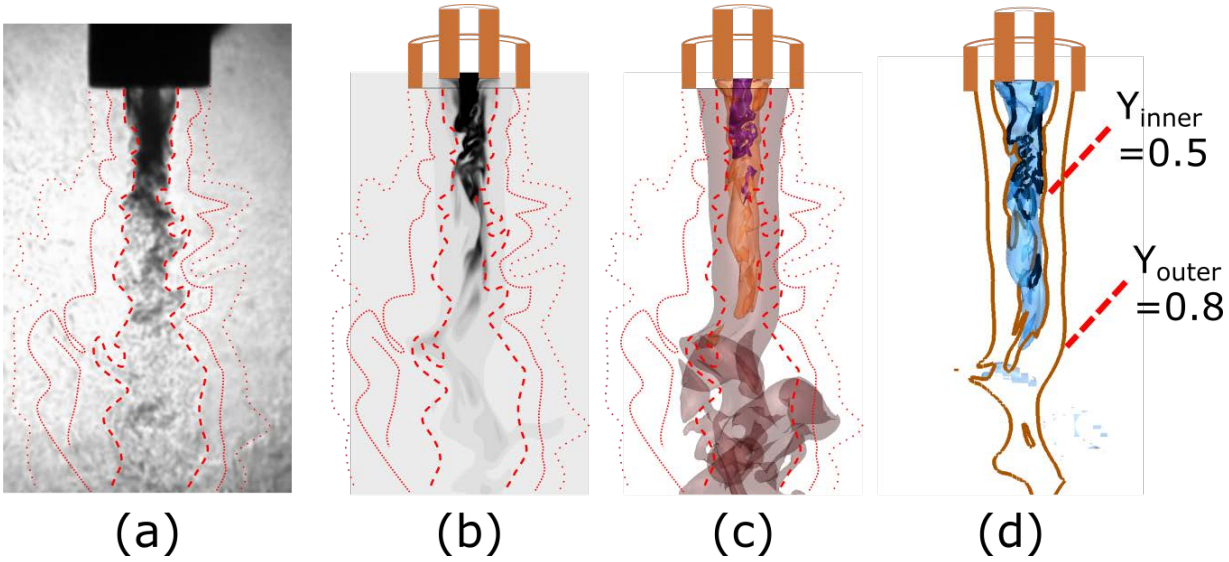

Figure 11. Details of the computed flowfield compared with the experimental image. Dark core region of the experimental shadowgraph (a) is not well represented by the center slice showing density (b). Isosurface of density (c) at 90, 180 and 300 kg/m^3 shows breakdown of the outer jet flow that presents dark regions beyond core flow. Iso-surface of the inner jet fluid at 50% mass fractions overlapping outer jet fluid mass fraction of 80% (d) shows mixing region beyond the dark core(black line).

D. Acoustic Excitation

Two cases are chosen to examine the impact of acoustic excitation on the mixing of the coaxial jets. The acoustic excitation is provided in this case by oscillating side walls with a specified frequency and phase. These walls are shown in **Figure 3**. For the pressure anti-node case, the phase difference is specified to be zero and the velocity of the walls is chosen so as to match the pressure fluctuation amplitude measured in the experiment. In the case of pressure node, the phase difference of the oscillating walls is 180^o and again, the velocity is chosen so as to match the known experimental pressure fluctuation levels. These conditions are summarized in **Table 1**.

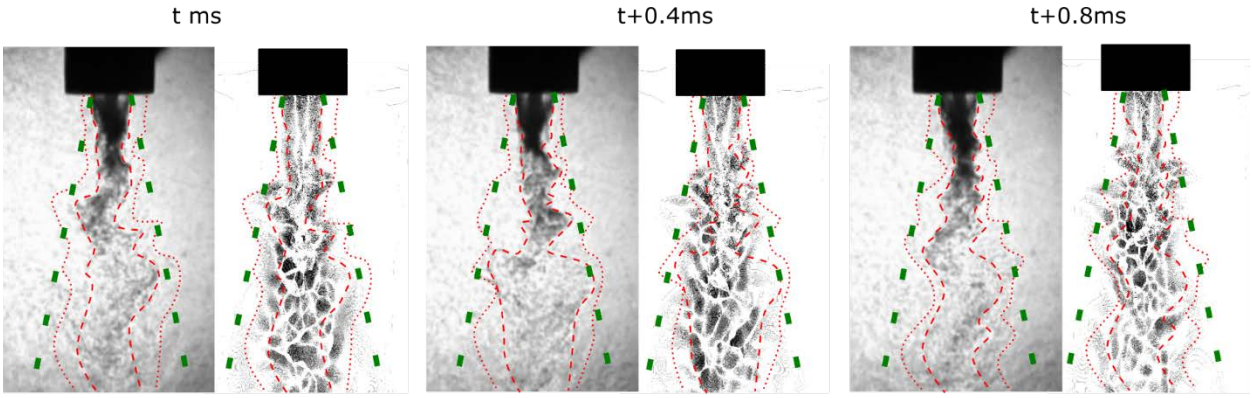

Figure 12. Comparison of the shadowgraph images from experiment and computations for the pressure anti-node case. Three instances that are ten frames apart are shown for comparison.

Pressure Anti-node Case:

In the previous section, the mixing of the co-axial jets is shown to extend beyond the length of the dark core apparent in the experimental images. It is therefore of interest to examine the acoustically excited case from a mixing standpoint. The pressure anti-node in the center plane leads to pressure fluctuations and the reduction of the dark core length can be attributed to these pressure fluctuations [7]. To understand this, the validity of the computations is first ascertained by comparing against the experimental images. Three time instances that are 10 frames or 0.4 ms apart are shown in **Figure 12**. Both the inner shear layer and the outer injector flow are marked on the experimental image and the profiles are superimposed on the computational images. Additionally, the spreading of the jet is marked by the green dashes in the experimental images and, for comparison, are carried over to the computational images. The comparison of the central region in all the three instances is close. The spreading rate is also found to be consistent between the two sets of images, indicating that the computations capture a behavior similar to the experiments.

Mixing of the two jets is viewed using 50% mass fraction iso-surface of the inner jet fluid along with an 80% mass fraction boundary of the outer jet. This is shown in **Figure 13**. The pressure fluctuations in this case cause upstream oscillations of both the inner and outer jets upstream compared to the baseline case. This confirms the experimental assessment based on the length of the dark core. However, the inner jet retains half the fluid beyond the observed dark core at "t" and t+0.4 ms, which is consistent with the baseline case. In the last of the snapshots, the length of the innjer jet is perceptibly shortened and slightly symmetric expansions appear with vortex shedding in the downstream region. Such vortex shedding is important in the case of combustion instability since the vortices can act as mixing elements and may augment coherency of the heat release, promoting thermo-acoustic coupling.

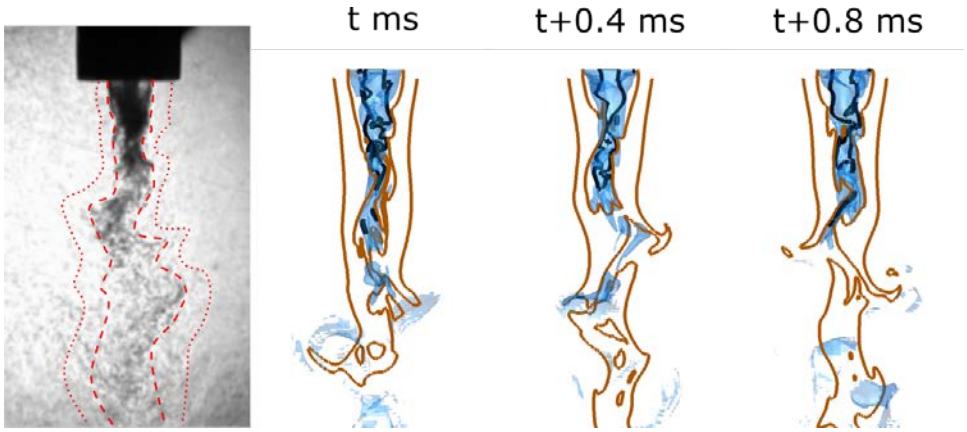

Figure 13. Pressure anti-node case, comparison of the shadowgraph image and the mixing of the jets. Iso-surface of the inner jet fluid is plotted at 50% mass fraction(blue) and the line contour gives 80% mass fraction of the outer jet fluid(brown line). Inner jet core is shown with 80% mass fraction of the inner jet fluid (black line).

Pressure Node Case:

The pressure node case corresponds to a velocity anti-node, implying that it may induce jet flapping at the center plane. At sub-critical pressures, the pressure node behavior is thought to eliminate toroidal vortex formation [22]. Presence of this behavior is investigated from the computational solution. First, the shadowgraph images are computed from the solutions and a comparison of the observed structures and the spreading rate is shown in **Figure 14**. Both the large scale structures as well as the spreading rate is seen to be consistent for the three consecutive time instances chosen.

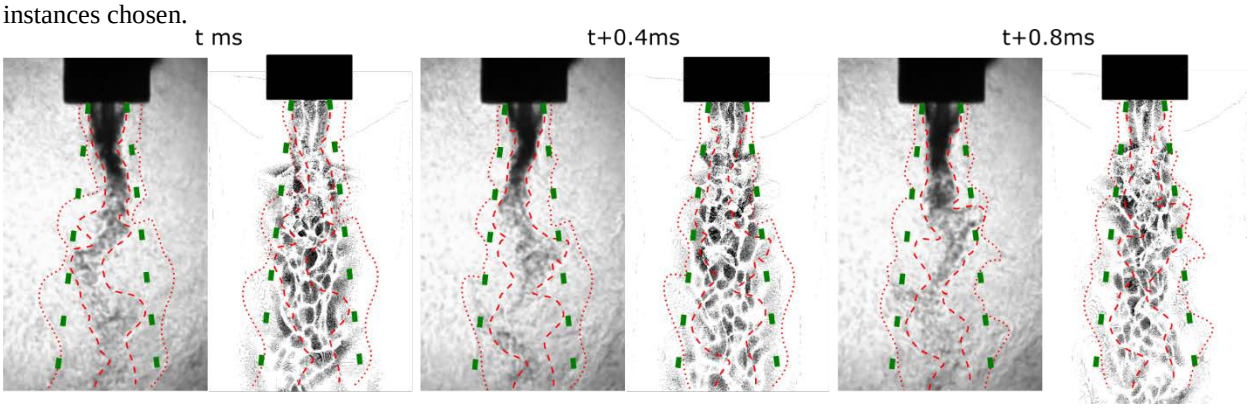

Figure 14. Comparison of the shadowgraph images from experiment and computations for the pressure anti-

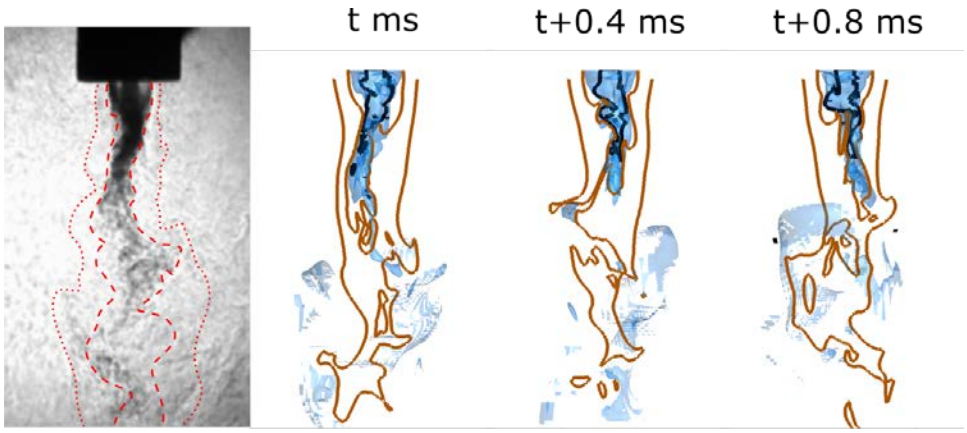

Figure 15. Pressure node case, comparison of the shadowgraph image and the mixing of the jets. Iso-surface of the inner jet fluid is plotted at 50% mass fraction(blue) and the line contour gives 80% mass fraction of the outer jet fluid(brown line). Inner jet core is shown with 80% mass fraction of the inner jet fluid (black line).

The mixing behavior is assessed in the same manner as the pressure anti-node case using the iso-surface and line contours of the inner and outer jet fluids. This behavior is shown in **Figure 15**. The observed inner jet behavior in this case is different than the pressure anti-node case. The velocity node at the center of the jets produces significant motion in both the jets that leads to complex evolution close to the length of the line contour corresponding to 80% inner jet fluid mass fraction seen from the baseline and the pressure anti-node case. This is shown in **Figure 16** using density iso-surfaces at 90, 180 and 280 kg/m^3. The flapping motion acts to shear both the jets at a location close to the injector tip, thereby increasing the mixing in the downstream section.

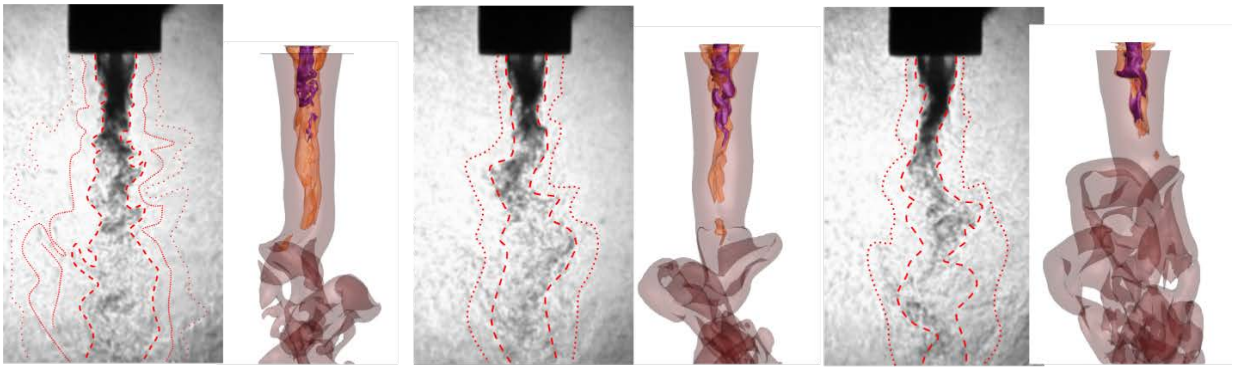

Figure 16. Experimental shadowgraph compared to density field for the three cases: baseline(a), pressure antinode(b) and pressure node(c). Large scale flapping motions result in shorter core for the pressure node case.

IV. Conclusions

Shear coaxial mixing of supercritical nitrogen with a jet momentum flux ratio of 1.5 is studied using computations and compared with the experimental data. The experimental measurements of the time-averaged temperature profile near the injector tip and back-lit images of the transient flowfield are compared against the computations. The mean temperature profile is found to be in reasonable agreement with the measurements. Comparison of the time-averaged images of the baseline case with the computationally averaged results from the center slice show that the density field is significantly dependent on the temperature field and is more representative of the experimental images.

Exploration of the transient flowfield, however, requires a more careful comparison that utilizes computationally generated shadowgraphs. Generating high contrast shadowgraphs from the solution data can be computationally intensive, but it vastly improves the quality and reliability of the validation. Although the experimental images contain the outer jet flow and outer shear layer, limited contrast makes it difficult to detect such features by automated procedures. Furthermore, the near-continuous presence of alternating dark and light spots that form a shadowgraph can be challenging to obtain a boundary of the salient features of the flowfield. The most important observation from this comparison is that the flow features seen in shadowgraph images are a function of the distance of the screen from the flowfield and therefore, may not truly represent the physics. This observation is further corroborated by the mixing analysis of the two jets.

Acoustically excited injector flow is studied for two cases representing pressure node and pressure anti-node forcing at the center plane of the injector. For both the cases, the computational shadowgraphs compare favorably with the experimental images, confirming the validity of the computations. The jet spreading rate is also reasonably captured for both the cases. Mixing analysis from the tagged inner and outer jet fluid indicates that the pressure node does not significantly shorten the high density inner core, but a slightly symmetric puffing is observed for the outer flow. For the pressure node case, on the other hand, a flapping motion is induced that acts to shear both the inner and outer jets closer to the injector tip. This results in a perceptible shortening of the high density core flow, generating vortices, that can be significant in studies of combustion instability.

The direct comparison of shadowgraph images from computations and experiment provides a semi-quantitative validation. A better validation can be obtained via data-based modeling techniques such as proper orthogonal decomposition (POD) and dynamic mode decomposition (DMD) [23, 24]]. Such techniques not only provide the statistical assessment of the fluid flow, but can also help identify the spatial structures that are responsible for the periodic phenomena. In general, they can provide a more quantitative basis for comparison of the predictions with experimental data and will be undertaken in the future.

Acknowledgement

The author would like to thank Dr. Talley for his suggestions and for the experimental information. The data provided and discussions with Dr. Munipalli of HyPerComp, Inc. are also acknowledged.

References

1. Oschwald, M., Smith, J. J., Branam, R., Hussong, J., Schik, A., Chehroudi, B., and Talley, D. "Injection of Fluids into Supercritical Environments," *Combustion Science and Technology* Vol. 178, No. 1-3, 2006, pp. 49-100.
doi: 10.1080/00102200500292464
2. Schmitt, T., Rodriguez, I. A., Leyva, I., and Candel, S. "Experiments and Numerical Simulation of Mixing Under Supercritical Conditions," Vol. 24, 2012.
3. Teshome, S., Leyva, I., and Talley, D. "Proper Orthogonal Decomposition Analysis of Shear-Coaxial Injector Flows with and Without Transverse Acoustic Forcing." Air Force Research Laboratory, Edwards AFB, 2011.
4. Mayer, W., Schik, A., Schaffler, M., and Tamura, H. "Injection and Mixing Processes in High-Pressure Liquid Oxygen/Gaseous Hydrogen Rocket Combustors," *Journal of Propulsion and Power* Vol. 16, No. 5, 2000, pp. 823-828.
doi: 10.2514/2.5647
5. Mayer, W., and Tamura, H. "Propellant injection in a liquid oxygen/gaseous hydrogen rocket engine," *Journal of Propulsion and Power* Vol. 12, No. 6, 1996, pp. 1137-1147.
doi: 10.2514/3.24154
6. Mayer, W., Telaar, J., Branam, R., Schneider, G., and Hussong, J. "Raman measurements of cryogenic injection at supercritical pressure," *Heat and Mass Transfer* Vol. 39, No. 8-9, 2003, pp. 709-719.
7. Leyva, I. A., Chehroudi, B., and Talley, D. "Dark core analysis of coaxial injectors at sub-, near-, and supercritical pressures in a transverse acoustic field," *43rd AIAA/ASME/SAE/ASEE Joint Propulsion Conference & Exhibit*. AIAA, Cincinnati, OH, 2007.
8. Rodriguez, I. J., Leyva, I. A., Chehroudi, B., and Talley, D. "Results on Subcritical One-Phase Coaxial Jet Spread Angles and Subcritical to Supercritical Acoustically-Forced Coaxial Jet Dark Core Lengths," *44th AIAA/ASME/SAE/ASEE Joint Propulsion Conference & Exhibit*. AIAA, Hartford, CT, 2008.
9. Selle, L., and Schmitt, T. "Large-Eddy Simulation of Single-Species Flows Under Supercritical Thermodynamic Conditions," *Combustion Science and Technology* Vol. 182, No. 4-6, 2010, pp. 392-404.
doi: 10.1080/00102200903462664
10. Liu, T., Zong, N., and Yang, V. "Dynamics of shear-coaxial cryogenic nitrogen jets with acoustic excitation under supercritical conditions," *44th AIAA aerospace sciences meeting and exhibit*. Reno, Nevada, 2006.
11. Hua, J.-C., Gunaratne, G. H., Talley, D. G., Gord, J. R., and Roy, S. "Dynamic-mode decomposition based analysis of shear coaxial jets with and without transverse acoustic driving," *Journal of Fluid Mechanics* Vol. 790, 2016, pp. 5-32.
doi: 10.1017/jfm.2016.2
12. Li, D., Sankaran, V., Lindau, J. W., and Merkle, C. L. "Computational Formulation for Multi-component and Multi-phase Flows," *43rd AIAA Aerospace Sciences Meeting and Exhibit, 2005*. AIAA, 2005.
13. Lian, C., Xia, G., and Merkle, C. L. "Impact of Source Terms on Reliability of CFD Algorithms," *Computers and Fluids*, 2010, pp. 1909-1922.
14. Venkateswaran, S., Lindau, J. W., Kunz, R. F., and Merkle, C. L. "Computation of Multiphase Mixture Flows with Compressibility Effects," *Journal of Computational Physics*, 2002, pp. 54-77.
15. Poling, B. E., Prausnitz, J. M., and O'Connell, J. P. *The Properties of Gases and Liquids*: McGraw-Hill, 2001.
16. Pedersen, K. S., and Christensen, P. L. *Phase Behavior of Petroleum Reservoir Fluids*: Taylor and Francis, 2007.
17. Soave, G. "Equilibrium Constants from a Modified Redlich-Kwong Equation of State," *Chemical Engineering Science* Vol. 27, 1972, pp. 1197-1203.
18. Lemmon, E. W., Huber, M. L., and McLinden, M. O. "NIST Standard Reference Database 23: Reference Fluid Thermodynamic and Transport Properties-REFPROP." National Institute of Standards and Technology, Standard Reference Data Program, Gaithersburg, 2013.
19. Yates, L. A. "Images constructed from computed flowfields," *AIAA Journal* Vol. 31, No. 10, 1993, pp. 1877-1884.
doi: 10.2514/3.11862
20. Saunders, D., and Kennelly, R. "CFD Utilities." Vol. 2016, 2014.
21. Morgan, C. J., Shipley, K. J., and Anderson, W. E. "Comparative Evaluation Between Experiment and Simulation for a Transverse Instability," *Journal of Propulsion and Power* Vol. 31, No. 6, 2015, pp. 1696-1706.
22. Graham, J., Leyva, I., Rodriguez, J., and Talley, D. "On the Effect of a Transverse Acoustic Field on a Flush Shear Coaxial Injector," *45th AIAA/ASME/SAE/ASEE Joint Propulsion Conference & Exhibit*. AIAA, Denver, Co, 2009.
23. Kutz, J. N. *Data-driven Modeling and Scientific Computation*: Oxford University Press, 2013.
24. Schmid, P. J. "Dynamic Mode Decomposition of Numerical and Experimental Data," Vol. 656, 2010, pp. 5-28.